Supporting information

Breaking the Selectivity-Activity Seesaw in Ethane Oxidative Dehydrogenation via the Synergetic Effects of Doping and Electrochemical Activation

Xiang Sun†[a], Benchi Chen†[a], Heejae Yang†[b], Mengzhen Zhou[a], Nian Zhang[c], Yunkyung Kim[d], Wonyoung Lee[e], Jeong Woo Han*[d], Zhang Lin[af] and Yan Chen*[a]

[a]*Guangdong Provincial Key Laboratory of Solid Wastes Pollution Control and Recycling, School of Environment and Energy, South China University of Technology, Guangzhou, 510006, China. E-mail: escheny@scut.edu.cn*

[b]*Department of Chemical Engineering, Pohang University of Science and Technology (POSTECH), Pohang, Gyeongbuk 37673, Republic of Korea.*

[c]*Shanghai Synchrotron Radiation Facility, Shanghai Advanced Research Institute, Chinese Academy of Sciences, Shanghai, 201204, China.*

[d]*Department of Materials Science and Engineering, Research Institute of Advanced Materials, Seoul National University, Seoul 08826, Republic of Korea. Email: jwhan98@snu.ac.kr*

[e]*SKKU Institute of Energy Science and Technology (SIEST), School of Mechanical Engineering, Sungkyunkwan University, Suwon, Gyeonggi-do 16419, Republic of Korea.*

[f]*Chinese National Engineering Research Center for Control & Treatment of Heavy Metal Pollution, School of Metallurgy and Environment, Central South University State Key Laboratory of Functional Materials for Informatics, Shanghai Institute of Microsystem and Information Technology, Chinese Academy of Sciences, Shanghai, 200050, China.*

† These authors contributed equally to this work.

Experiments

Material synthesis and cell fabrication

Solid-phase reaction method was used to prepare double perovskite $Sr_2Ti_{0.8}CoO_{6-\delta}$(STC), $Sr_2Ti_{0.8}Co_{0.6}Fe_{0.6}O_{6-\delta}$(STCF), and $Sr_2Ti_{0.8}FeO_{6-\delta}$(STF) electrode material powders with different Fe/Co ratios, and the three materials were prepared by basically the same method, only changing $SrCO_3$, TiO_2, Co_3O_4 and Fe_2O_3 (Macklin, China) stoichiometric ratios, and then mixed with appropriate amount of ethanol and then ball milled for 24 h. The dried mixture was calcined in a muffle furnace for 8 h at 1200 ºC.

The $La_{0.8}Sr_{0.2}Ga_{0.83}Mg_{0.17}O_{3-\delta}$ (LSGM) electrolyte was synthesized by mixing powders of La_2O_3, MgO, $SrCO_3$ and Ga_2O_3 with ethanol and being ball-milled for 24 h. The obtained LSGM mixture was pressed into a pellet and pre-sintered at 1250 ºC for 10 h. The obtained pellet was ground into powder and were then pressed into pellet again. After further sintering at 1450 °C for 10 h, the LSGM electrolyte support was successfully prepared.

The electrode slurry was prepared by mixing electrode material powders and graphite in a weight ratio of 10:2 with a binder composed of α-terpineol and Polyvinyl Butyral, followed by grounding with mortar for 3 h. The STCF cathodes and anodes (STC, STCF and STF) were fabricated by printing the slurry onto both sides of the LSGM electrolyte support. After sintering at 1150 °C for 3 h, the complete electrolyte-supported single cell was finally achieved, denoted as STCF/LSGM/STC,STCF and STF. The electrode effective area of every cell was 0.5 cm^2.

Pulsed laser deposition (PLD) was used for preparing the thin film cell in this work. The PLD targets were acquired by pressing the corresponding powders into pellets and then sinter at 1300 °C for 6 h. A thin layer of STC, STCF and STF electrode was deposited on single crystal yttria stabilized zirconia (YSZ) substrate by PLD using a KrF excimer laser with laser energy of 300 mJ and wavelength of 248 nm. The deposition was carried out at 600 °C under the oxygen pressure of about 1 Pa. The distance from PLD targets to substrates was set to be 6 cm. After deposition, thin-film samples were cooled down to room temperature with the rate of 5 °C min^{-1} under oxygen pressure of 200 Pa. A thin layer of gadolinium-doped cerium oxide (GDC) was deposited between STC, STCF and STF films and YSZ electrolyte as a buffer layer.

Electrochemical measurements and gas product analysis

For the electrochemical measurement, while the cathode electrode side was fed with pure CO_2 with a flow rate of 20 mL min^{-1}, the mixture of C_2H_6/Ar was supplied to the anode side. The flow rate is controlled to be 16 mL min^{-1} for Ar and 4 mL min^{-1} for ethane, giving a total flow rate of 20 mL min^{-1} (20 percent ethane). All gas flows are precisely controlled by mass flow meters (Alicat, USA).

Electrochemical tests were performed on the electrochemical workstation (IM6, Zahner, Germany). The composition of the reaction products was analyzed using gas chromatography (GC9790II, Fuli Instruments). Two different Hydrogen Flame Ionization Detector (FID) detectors in our chromatography system (GC9790II model from Zhejiang Fuli Instruments, China) for detecting CO/CO2 (FID I) and CH4/C2H6/C2H4 (FID2) respectively. A methanator (catalytic conversion module) is incorporated into the FID2 detectors to enable the detection of CO and CO_2. The conversion of ethane (C_{C2H6}) and the selectivity of products (S_i) were calculated following the equations:

$$[C]_{total} = [CH_4] + [CO] + [CO_2] + 2[C_2H_4] + 2[C_2H_6]$$

$$C_{C2H6} = 1 - 2[C_2H_6]/[C]_{total}$$

$$S_{C2H4} = 2[C_2H_4] /([C]_{total} - 2[C_2H_6])$$

$$S_{CH4} = [CH_4] /([C]_{total} - 2[C_2H_6])$$

$$S_{CO} = [CO] /([C]_{total} - 2[C_2H_6])$$

$$S_{CO2} = [CO_2] /([C]_{total} - 2[C_2H_6]) \text{ “}$$

where $[C]_{total}$ is the total amount of C in the exit gas. $[CH_4]$, $[CO]$, $[CO_2]$, $[C_2H_4]$, and $[C_2H_6]$ are the amounts of methane, carbon monoxide, carbon dioxide, ethylene, and ethane in the exit gas.

Thermogravimetric test

The samples tested were placed on a test bench and heated up to 900 ºC at 10 $_o$C-min^{-1} under N_2 atmosphere and the change in weight of the material was recorded.

Programmed warming reduction/desorption test

O_2-TPD test: The sample was placed in a test tube and pretreated at 300 ºC and He gas. Adsorption was carried out by passing 30% O_2/He mixture for 1 h at 50 ºC, then switched to He gas flow for purging, and after the baseline was stabilized, the temperature was raised to 500 ºC, and the stripped gas was detected by TCD.

Material characterizations

The crystal structure of the materials was analyzed by X-ray diffraction (XRD, Bruker D8 Advance, Germany) with Cu-Kα radiation. High resolution X-ray diffraction (HRXRD, Rigaku, Japan) with Cu-Kα radiation was used to characterize the crystal structure and lattice constants of the thin film system. The topography was investigated by scanning electron microscopy (SEM, SU8010, Hitachi, Japan). The microstructure and local composition were probed by transmission electron microscopy (TEM) which was coupled with energy dispersive X-ray spectroscopy (EDS) analysis (JEM 2100F, JEOL, Japan) operating at 200 kV.

Density Functional Theory Calculations

All theoretical studies were performed by spin-polarized density functional theory (DFT) with the Vienna ab Initio Simulation Package (VASP)[1, 2]. The projected-augmented wave (PAW) pseudopotentials were utilized to address the core electrons, and a plane-wave kinetic energy cutoff was set to 400 eV[3, 4]. The generalized gradient approximation (GGA) proposed by Perdew, Burke and Ernzerhof (PBE) was used for the exchange-correlation energies[5].

To reduce the computational time, Sr_2TiCoO_6, $Sr_2TiCo_{0.5}Fe_{0.5}O_6$, and Sr_2TiFeO_6 models were created for the STC, STCF, and STF chalcogenide calculations. For the

Brillouin zone of the bulk and flat plate models, 6 × 6 × 6 and 3 × 3 × 1 Monkhorst Pack k-points, respectively, were used for sampling. For DOS calculations, 13 × 13 × 13 Monkhorst Pack k-point sampling was used. Based on our experimental characterization and the model of Ref. The chalcogenide BO_2 capped (001) flat plate structure consists of 8 layers (the bottom 3 layers are fixed) and ~20 Å vacuum spacing in the direction perpendicular to the surface. GGA+U approach was used to correct the significant self-interaction, and U_{eff} was added to the open-shell d-electrons, 4.4 eV for Ti, 4.0 eV for Fe and 3.4 eV for Co[6, 7]. The converge criterion of the energy was 1×10^{-5} eV for the self-consistent-field (SCF) iterations. Based on a force-based conjugated gradient algorithm, geometries were relaxed until the forces on each atom were within 0.03 eV/Å. The Janak-Slater (JS) transition state method was used to calculate the core level energy, which considers the half occupancy of the core level when estimating the O 1s binding energies (BEs).[8, 9] The BEs were determined by reference to the vacuum energy level, which was determined by the VASPKIT 426 function as the electrostatic potential energy. The Gibbs free energy was calculated with zero-point energy and entropy as follows:

$$\Delta G = \Delta E + \Delta ZPE - T\Delta S,$$

where E is the DFT-calculated energy, ZPE is the zero-point energy, T is the temperature, 1073K and S is the entropy. We assume that the entropy of the adsorbed species is zero. The NIST database was used to obtain the standard entropy of gas molecules[10]. For the ZPE correction, we calculated the vibration frequencies by using the density functional perturbation theory.

The p-band center was calculated by

$$\varepsilon_p = \frac{\int_{-\infty}^{\infty} E\rho(E)dE}{\int_{-\infty}^{\infty} \rho(E)dE},$$

where E is the energy, E_f is the Fermi-level energy, and ρ is density of state. The adsorption energy of H* ($\Delta E_{ads,\,H}$) was calculated by

$$\Delta E_{ads,\,H} = E_{H*} - E_{slab} - 1/2E_{H2},$$

in which E_{H2}, E_{slab} are the energies for gaseous H_2, pristine slab model and E_{H*} is the total energy of the slab model when the H* is adsorbed on the lattice oxygen. The adsorption energy of C_2H_5* was derived from the following equation:

$\Delta E_{ads, C2H5} = E_{C2H5*} - E_{slab} - (E_{C2H6} - 1/2E_{H2})$,

where E_{C2H5*} is the total energy of the slab model when the C_2H_5* is adsorbed on the surface, E_{C2H6} is the energies for gaseous C_2H_6. The oxygen vacancy formation energy (E_{Ov}) was calculated from the total energies of each slab models,

$E_{Ov} = (E_{Vo} + 1/2E_{O2}) - E_{slab}$,

where E_{Ov} is the total energy of the system containing an oxygen vacancy, and E_{O2} is the energies for gaseous O_2.

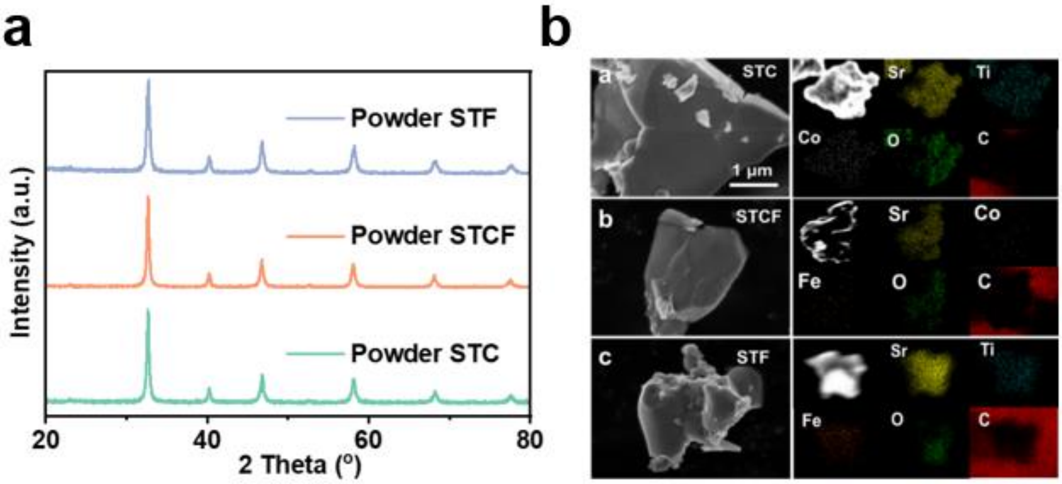

Figure S1. (a) XRD patterns and **(b)** SEM image and EDS spectra of STF, STCF and STC powder.

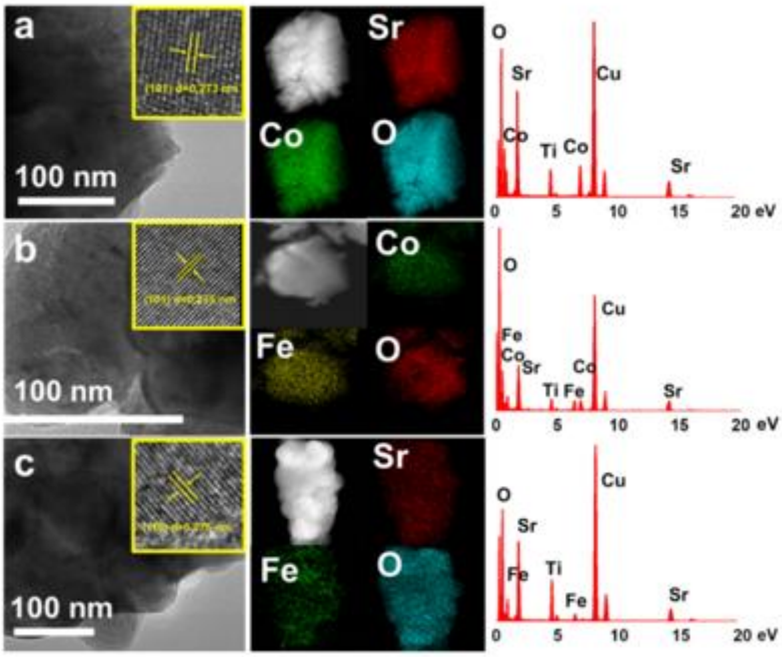

Figure S2. (a-c) TEM image and EDS spectra of STC, STCF and STF powder.

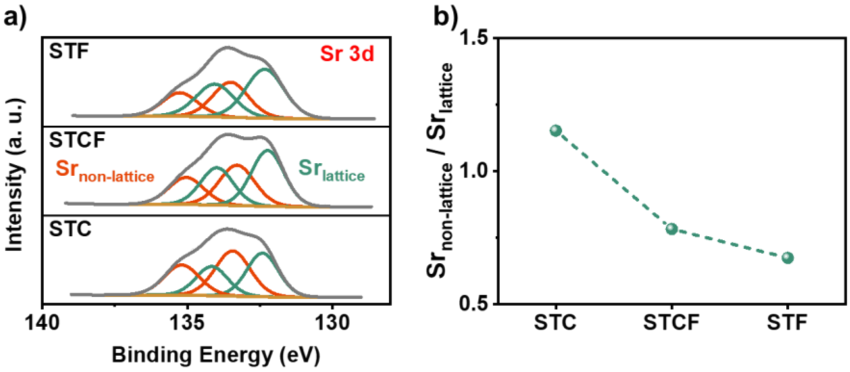

Figure S3. XPS spectra of Sr 3*d* (a,b) of STC, STCF and STF.

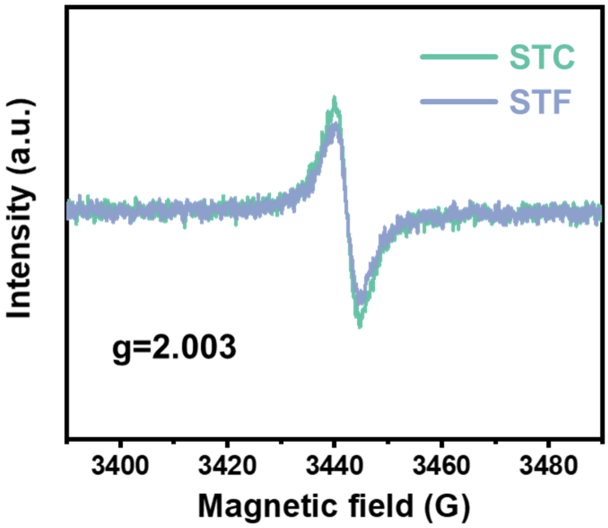

Figure S4. EPR spectra of STC, STF samples.

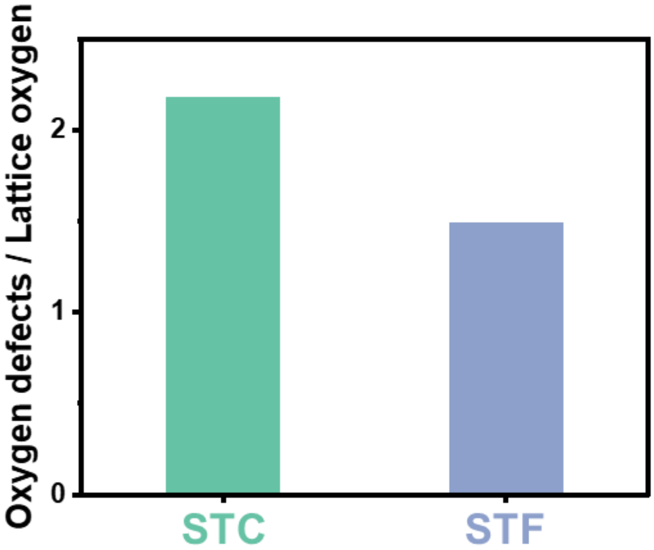

Figure S5. Oxygen Defect/Lattice Oxygen for STC and STF

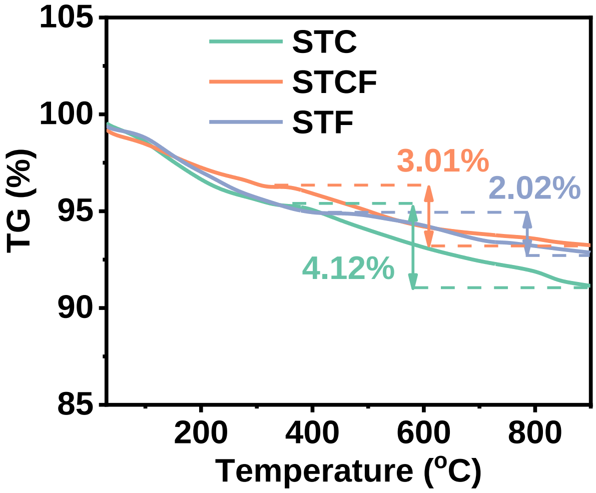

Figure S6. N_2-TG curves for STC, STCF and STF.

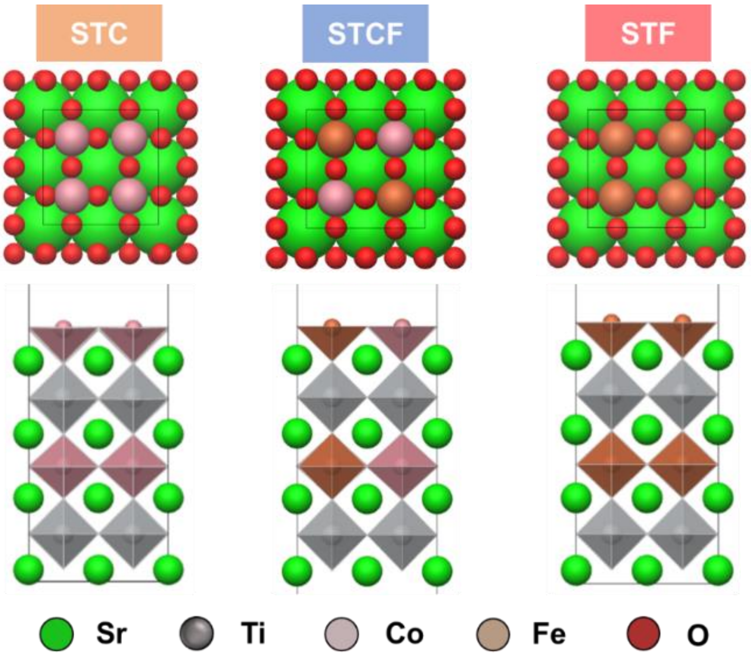

Figure S7. Three modeling systems, named STC, STCF, and STF.

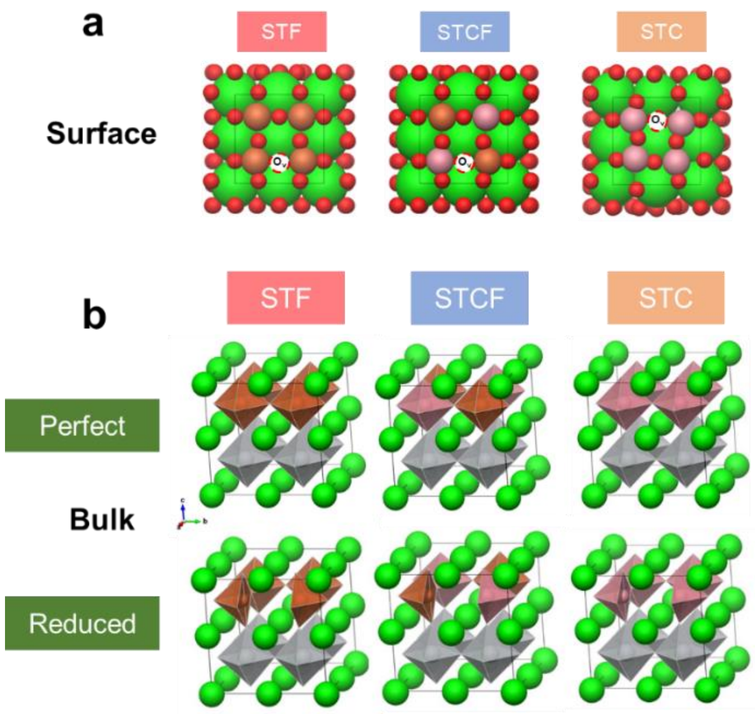

Figure S8. Model diagram of oxygen vacancy formation energy for surface (a) and bulk phase (b) in three model systems.

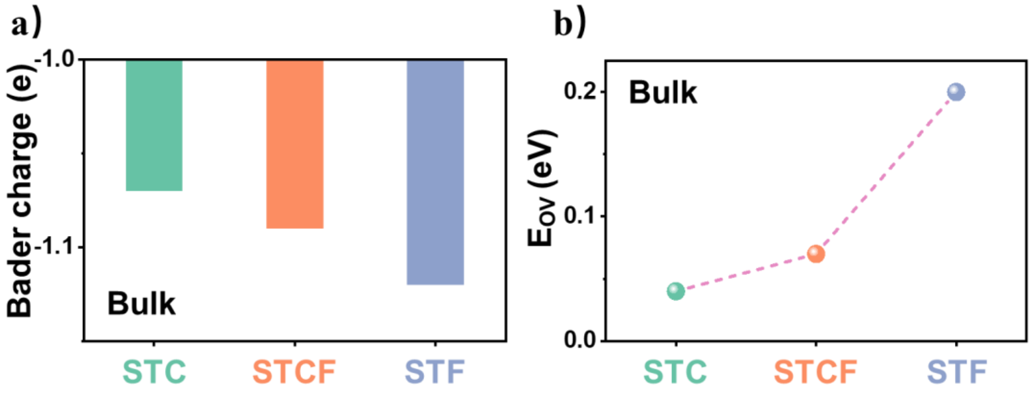

Figure S9. (a) bulk electronic structure of oxygen; (b) Oxygen vacancy formation energy for bulk phase in three model systems (STC, STCF, and STF).

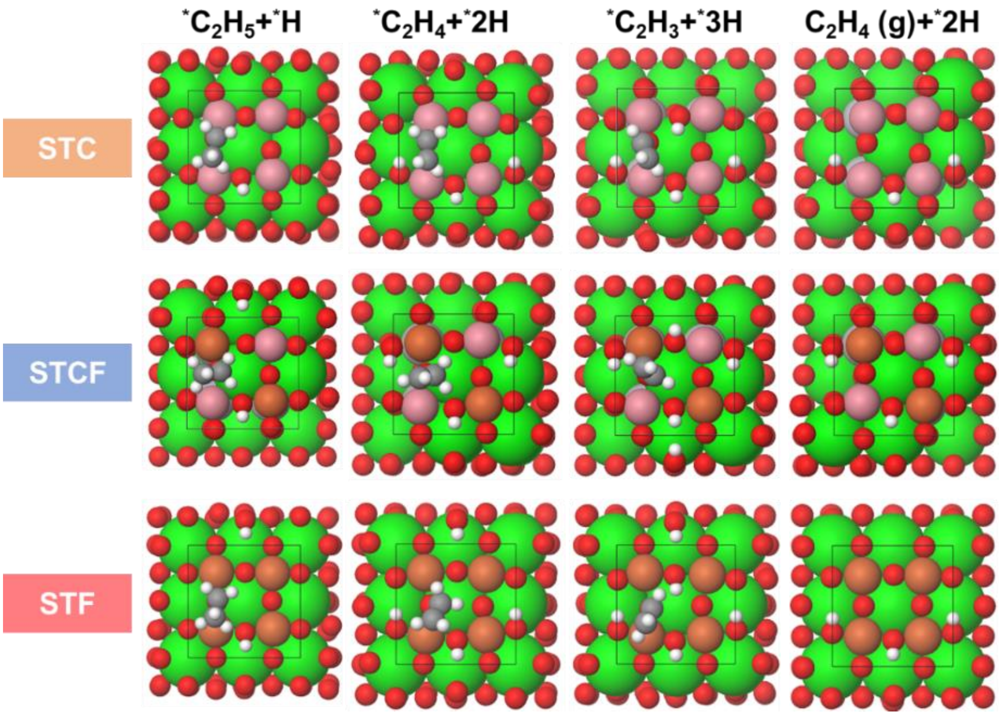

Figure S10. The configuration of reaction intermediate of ethane dehydrogenation pathways on the three systems (STC, STCF and STF).

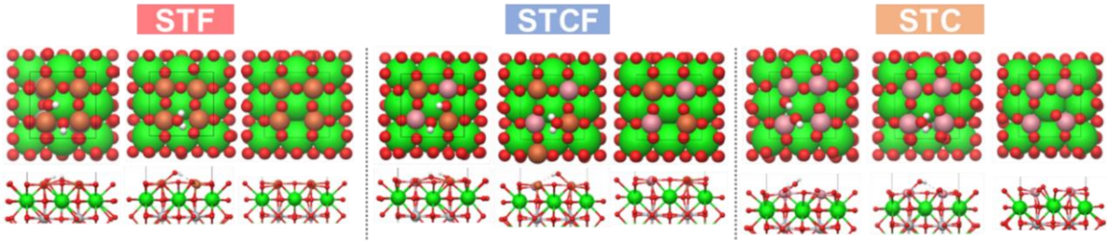

Figure S11. The configuration of the H_2O formation and desorption pathways on the three systems.

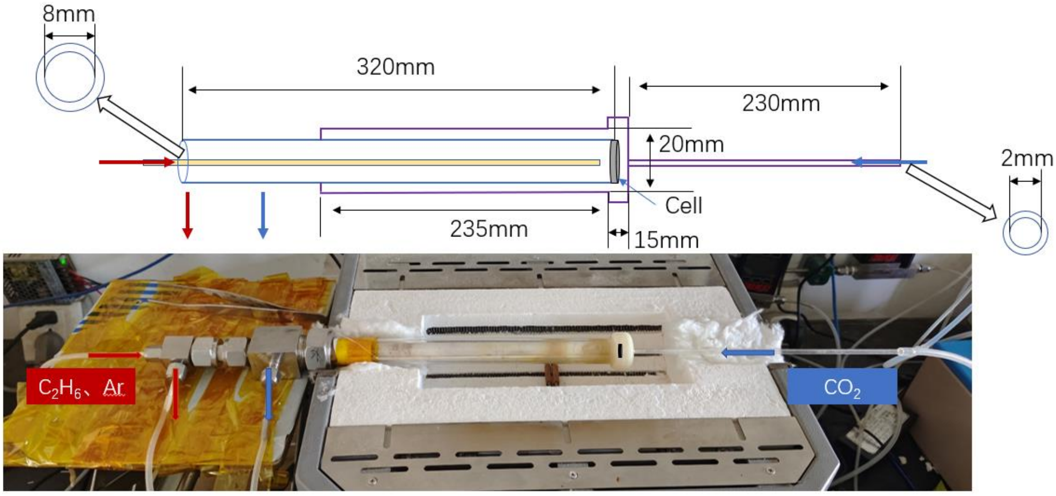

Figure S12. Schematic and physical photograph of the reactor used for electrochemical testing.

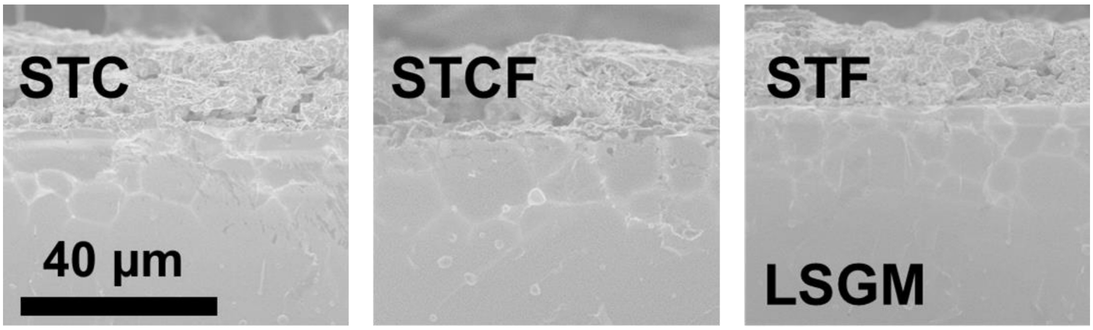

Figure S13. SEM images of anode and electrolyte for three different anode materials (STC, STCF, STF).

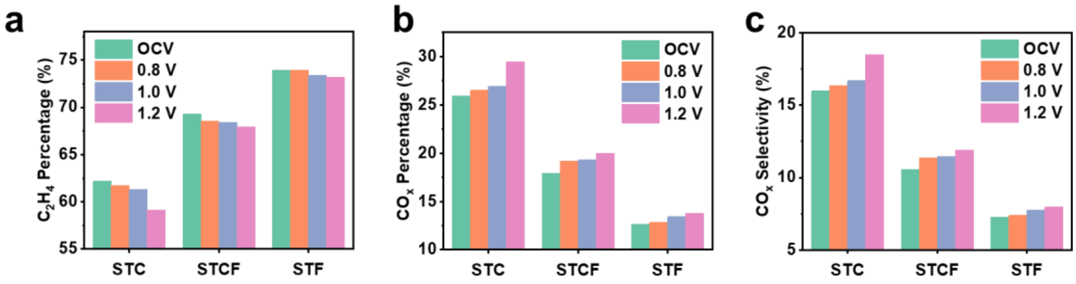

Figure S14. Proportion of C_2H_4 **(a)** and CO_x **(b)** gas composition; CO_x **(c)** selectivity in three types of cells anode products with different anode materials (STC, STCF, and STF) with a 20%C_2H_6/Ar flow rate of 20 mL·min^{-1}.

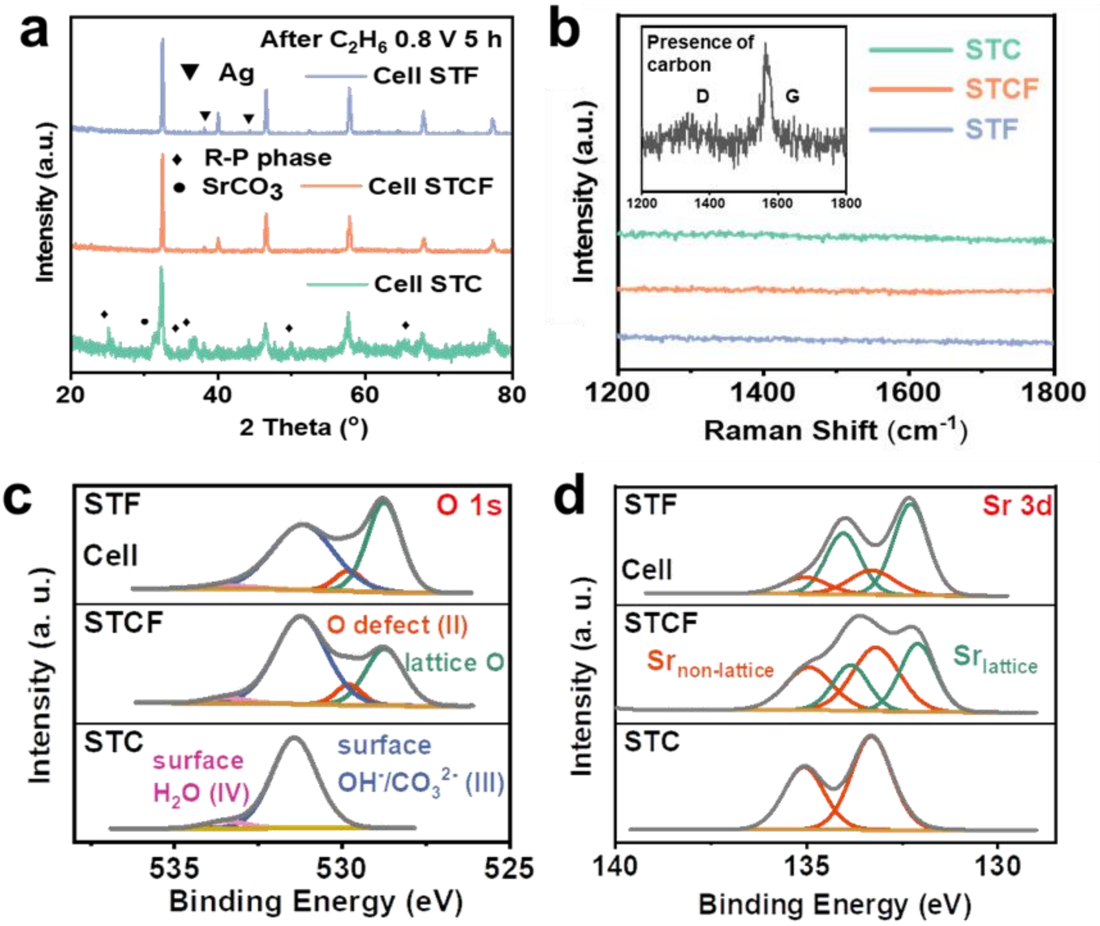

Figure S15. **(a)** XRD pattern, **(b)** Raman spectra (inset shows Raman spectra of graphite), XPS spectra of **(c)** O 1*s* and **(d)** Sr 3*d* of anode side electrode material (STC, STCF, and STF) after electrolytic testing for 300 min of powder cells at 0.8 V with a 20% C_2H_6/Ar flow rate of 20 mL·min^{-1}.

Table S1. O 1s XPS peak deconvolution results.

Sample	Lattice oxygen	Oxygen defects	Surface OH^- /CO_3^{2-}	Surface H_2O	Oxygen defects/Lattice oxygen
STC	11.31	24.75	58.45	5.48	2.18
STCF	17.04	27.10	51.22	4.62	1.59
STF	17.50	26.16	50.27	6.06	1.49

Table S2. Comparison of the performance of ethane oxide dehydrogenation using carbon dioxide as an oxidant in this work with other reported results.

No.	Reactant	Catalyst	Conversion (%)	Selectivity (%)	Temperature (ºC)	Yield (%)	Ref.
1	C_2H_6+CO_2	γ-$Al_2O_3/La_{0.6}Sr_{0.4}Co_{0.2}Fe_{0.8}O_{3-\delta}$ (SOEC)	5.9	90	600	5.3	11
2	C_2H_6+CO_2	Pt, Sn/Mg(Al)O	6.1	98.7	600	6.0	12
3	C_2H_6+CO_2	VO_x/Al_2O_3-ZrO_2	8.5	82	525	6.9	13
4	C_2H_6+CO_2	MoO_x/Al_2O_3	10	85	600	8.5	14
5	C_2H_6+CO_2	Fe/NiO-MgO-ZrO_2	11.9	79	600	9.4	15
6	C_2H_6+CO_2	CeO_2 (SOEC)	10	95	600	9.5	16
7	C_2H_6+CO_2	$La_{0.2}Sr_{0.8}TiO_{3\pm d}Cl_\sigma$ (SOEC)	14	71.4	600	10.0	17
8	C_2H_6+CO_2	Fe/Mo_2C	14	80	600	11.2	18
9	C_2H_6+CO_2	CrO_x/Al_2O_3	14	90	700	12.6	19
10	C_2H_6+CO_2	CeO_2	14	95	750	13.3	20
11	C_2H_6+CO_2	NiAl	26.2	52.5	700	13.7	21
12	C_2H_6+CO_2	Ni-Nb-Cr-O	26	65	450	16.9	22
13	C_2H_6+CO_2	Ga_2O_3	19.6	95	650	18.6	23
14	C_2H_6+CO_2	LSF@10Li_2CO_3	29	75.5	720	21.9	24
15	C_2H_6+CO_2	Cr_2O_3-ZSM-5 (membrane reactor)	43	80	750	34.4	25
16	C_2H_6+CO_2	Fe_3Ni_1/CeO_2	67.3	63.5	800	42.7	26
17	C_2H_6+CO_2	Co-$BaCO_3$	48	92.2	650	44.2	27
18	C_2H_6+CO_2	Ca-ThO_2	46	97	725	44.6	28
19	C_2H_6+CO_2	Cr/TS(30)	52.7	90	650	47.4	29
20	C_2H_6+CO_2	Co-Cr_2O_3/ZrO2	61	80	650	48.8	30
21	C_2H_6+CO_2	Cr/H-ZSM-5	70	70	650	49	31
22	C_2H_6+CO_2	$CoO_x/MgAl_2O_4$-HT	55.2	89.5	650	49.4	32
23	C_2H_6+CO_2	Li-promoted $La_xSr_{2-x}FeO_{4-\delta}$	61	90	700	54.9	33
24	C_2H_6+CO_2	$Zn_{2.92}$/NaS50	70	90	650	63	34
25	C_2H_6+CO_2	$Sr_2Ti_{0.8}Co_{0.6}Fe_{0.6}O_{6-\delta}$	76.6	86.5	800	66.2	35
26	**C_2H_6+CO_2**	**STF (SOEC)**	**83.5**	**84.5**	**800**	**70.6**	**This work**

Reference

1. Kresse, G.; Hafner, J., Ab initio molecular dynamics for liquid metals. *Phys. Rev. B* **1993,** *47* (1), 558-561.

2. Kresse, G.; Furthmuller, J., Efficient iterative schemes for ab initio total-energy calculations using a plane-wave basis set. *Phys. Rev. B* **1996,** *54* (16), 11169-11186.

3. Blochl, P. E., Projector augmented-wave method. *Phys. Rev. B* **1994,** *50* (24), 17953-17979.

4. Kresse, G.; Joubert, D., From ultrasoft pseudopotentials to the projector augmented-wave method. *Phys. Rev. B* **1999,** *59* (3), 1758-1775.

5. Perdew, J. P.; Burke, K.; Ernzerhof, M., Generalized gradient approximation made simple. *Phys. Rev. Lett.* **1996,** *77* (18), 3865-3868.

6. Klyukin, K.; Alexandrov, V., Effect of intrinsic point defects on ferroelectric polarization behavior of $SrTiO_3$. *Phys. Rev. B* **2017,** *95* (3), 035301.

7. Kwon, O.; Sengodan, S.; Kim, K.; Kim, G.; Jeong, H. Y.; Shin, J.; Ju, Y. W.; Han, J. W.; Kim, G., Exsolution trends and co-segregation aspects of self-grown catalyst nanoparticles in perovskites. *Nat. Commun.* **2017,** *8* (1), 15967.

8. Janak, J. F., Proof that $\partial E/\partial n_i=\varepsilon$ in density-functional theory. *Phys. Rev. B* **1978,** *18* (12), 7165-7168.

9. Pueyo Bellafont, N.; Viñes, F.; Hieringer, W.; Illas, F., Predicting core level binding energies shifts: Suitability of the projector augmented wave approach as implemented in VASP. *J. Comput. Chem.* **2017,** *38* (8), 518-522.

10. P.J. Linstrom, W. G. M., NIST chemistry webbook, NIST standard reference database number 69, national Institute of standards and technology. **2022**, Gaithersburg MD, 20899.

11. Wu, T.; Sun, S.; Song, J.; Xi, S.; Du, Y.; Chen, B.; Sasangka, W. A.; Liao, H.; Gan, C. L.; Scherer, G. G.; Zeng, L.; Wang, H.; Li, H.; Grimaud, A.; Xu, Z. J., Iron-facilitated dynamic active-site generation on spinel $CoAl_2O_4$ with self-termination of surface reconstruction for water oxidation. *Nat. Catal.* **2019,** *2* (9), 763-772.

12. Virnovskaia, A.; Rytter, E.; Olsbye, U., Kinetic and isotopic study of ethane dehydrogenation over a semicommercial Pt, Sn/Mg(Al)O Catalyst. *Ind. Eng. Chem. Res.* **2008,** *47* (19), 7167-7177.

13. Elbadawi, A. H.; Ba-Shammakh, M. S.; Al-Ghamdi, S.; Razzak, S. A.; Hossain, M. M.; de Lasa, H. I., Phenomenologically based kinetics of ODH of ethane to ethylene using lattice oxygen of $VO_x/Al_2O_3–ZrO_2$ catalyst. *Chem. Eng. Res. Des.* **2017,** *117*, 733-745.

14. Yao, R.; Herrera, J. E.; Chen, L.; Chin, Y.-H. C., Generalized mechanistic framework for ethane dehydrogenation and oxidative dehydrogenation on molybdenum oxide catalysts. *ACS Catal.* **2020,** *10* (12), 6952-6968.

15. Theofanidis, S. A.; Loizidis, C.; Heracleous, E.; Lemonidou, A. A., CO_2-oxidative ethane dehydrogenation over highly efficient carbon-resistant Fe-catalysts. *J. Catal.* **2020,** *388*, 52-65.

16. Ye, L.; Duan, X.; Xie, K., Electrochemical oxidative dehydrogenation of ethane to ethylene in a solid oxide electrolyzer. *Angew. Chem. Int. Edit.* **2021,** *60* (40), 21746-21750.

17. Dogu, D.; Meyer, K. E.; Fuller, A.; Gunduz, S.; Deka, D. J.; Kramer, N.; Co, A. C.; Ozkan, U. S., Effect of lanthanum and chlorine doping on strontium titanates for the electrocatalytically-assisted oxidative dehydrogenation of ethane. *Appl. Catal. B: Environ.* **2018,** *227*, 90-101.

18. Yao, S.; Yan, B.; Jiang, Z.; Liu, Z.; Wu, Q.; Lee, J. H.; Chen, J. G., Combining CO_2

reduction with ethane oxidative dehydrogenation by oxygen-modification of molybdenum carbide. *ACS Catal.* **2018,** *8* (6), 5374-5381.

19. Bugrova, T. A.; Dutov, V. V.; Svetlichnyi, V. A.; Cortés Corberán, V.; Mamontov, G. V., Oxidative dehydrogenation of ethane with CO_2 over CrO_x catalysts supported on Al_2O_3, ZrO_2, CeO_2 and $CexZr_{1-x}O_2$. *Catal Today* **2019,** *333*, 71-80.

20. Valenzuela, R. X.; Bueno, G.; Cortés Corberán, V.; Xu, Y.; Chen, C., Selective oxidehydrogenation of ethane with CO_2 over CeO_2-based catalysts. *Catal Today* **2000,** *61* (1), 43-48.

21. Sagar, T. V.; Surendar, M.; Padmakar, D.; Parameswaram, G.; Lingaiah, N.; Rao, K. S. R.; Reddy, I. A. K.; Sumana, C.; Prasad, P. S. S., Selectivity reversal in oxidative dehydrogenation of ethane with CO_2 on CaO–NiO/Al_2O_3 catalysts. *Catal.Lett.* **2017,** *147* (1), 82-89.

22. Qiao, A.; Kalevaru, V. N.; Radnik, J.; Martin, A., Oxidative dehydrogenation of ethane to ethylene over Ni–Nb–M–O catalysts: Effect of promoter metal and CO_2-admixture on the performance. *Catal Today* **2016,** *264*, 144-151.

23. Nakagawa, K.; Okamura, M.; Ikenaga, N.; Suzuki, T.; Nakagawa, K.; Okamura, M.; Suzuki, T.; Kobayashi, T.; Kobayashi, T., Dehydrogenation of ethane over gallium oxide in the presence of carbon dioxide. *Chem. Commun.* **1998,** (9), 1025-1026.

24. Gao, Y.; Wang, X.; Liu, J.; Huang, C.; Zhao, K.; Zhao, Z.; Wang, X.; Li, F., A molten carbonate shell modified perovskite redox catalyst for anaerobic oxidative dehydrogenation of ethane. *Sci. Adv.* **2020,** *6* (17), eaaz9339.

25. Zhang, P.; Tong, J.; Huang, K., Role of CO_2 in catalytic ethane-to-ethylene conversion using a high-temperature CO_2 transport membrane reactor. *ACS Sustain. Chem. Eng.* **2019,** *7* (7), 6889-6897.

26. Xie, Z.; Xu, Y.; Xie, M.; Chen, X.; Lee, J. H.; Stavitski, E.; Kattel, S.; Chen, J. G., Reactions of CO_2 and ethane enable CO bond insertion for production of C_3 oxygenates. *Nat. Commun.* **2020,** *11* (1), 1887.

27. Zhang, X.; Ye, Q.; Xu, B.; He, D., Oxidative dehydrogenation of ethane over Co–$BaCO_3$ catalysts using CO_2 as oxidant: effects of Co promoter. *Catal. Lett.* **2007,** *117* (3), 140-145.

28. Baidya, T.; van Vegten, N.; Baiker, A., Selective conversion of ethane to ethene via oxidative dehydrogenation over Ca-doped ThO_2 using CO_2 as oxidant. *Top. Catal.* **2011,** *54* (13), 881.

29. Zhao, X.; Wang, X., Oxidative dehydrogenation of ethane to ethylene by carbon dioxide over Cr/TS-1 catalysts. *Catal. Commun.* **2006,** *7* (9), 633-638.

30. Deng, S.; Li, H.; Li, S.; Zhang, Y., Activity and characterization of modified Cr_2O_3/ZrO_2 nano-composite catalysts for oxidative dehydrogenation of ethane to ethylene with CO_2. *J. Mol. Catal. A: Chem.* **2007,** *268* (1), 169-175.

31. Mimura, N.; Takahara, I.; Inaba, M.; Okamoto, M.; Murata, K., High-performance Cr/H-ZSM-5 catalysts for oxidative dehydrogenation of ethane to ethylene with CO_2 as an oxidant. *Catal. Commun.* **2002,** *3* (6), 257-262.

32. Zhang, X., Hydrothermal synthesis and catalytic performance of high-surface-area mesoporous nanocrystallite $MgAl_2O_4$ as catalyst support. *Mater. Chem. Phys.* **2009,** *116* (2), 415-420.

33. Gao, Y.; Neal, L. M.; Li, F., Li-promoted $La_xSr_{2-x}FeO_{4-\delta}$ core–shell redox catalysts for oxidative dehydrogenation of ethane under a cyclic redox scheme. *ACS Catal.* **2016,** *6* (11), 7293-7302.

34. Liu, J.; He, N.; Zhang, Z.; Yang, J.; Jiang, X.; Zhang, Z.; Su, J.; Shu, M.; Si, R.;

Xiong, G.; Xie, H.-b.; Vilé, G., Highly-dispersed zinc species on zeolites for the continuous and selective dehydrogenation of ethane with CO_2 as a soft oxidant. *ACS Catal.* **2021,** *11* (5), 2819-2830.

35. Sun, X.; Yang, H.; Chen, B.; Zhou, M.; Ye, Y.; Li, X.; Zhang, H.; Yu, B.; Li, Y.; Han, J. W.; Chen, Y., Electrochemical Activation of Surface Oxygen for Efficient Oxidative Dehydrogenation Reaction at Elevated Temperatures. *ACS Catalysis* **2024,** *14* (8), 5827-5837.